Developmental Cognitive Neuroscience 64 (2023) 101314

Contents lists available at ScienceDirect

Developmental Cognitive Neuroscience

journal homepage: www.elsevier.com/locate/dcn

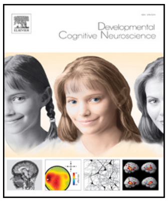

Structural and functional connectome relationships in early childhood

Yoonmi Hong [a,*], Emil Cornea [a], Jessica B. Girault [a,b], Maria Bagonis [a], Mark Foster [a], Sun Hyung Kim [a], Juan Carlos Prieto [a], Haitao Chen [c], Wei Gao [c], Martin A. Styner [a,d], John H. Gilmore [a]

[a] *Department of Psychiatry, University of North Carolina at Chapel Hill, United States of America*
[b] *Carolina Institute for Developmental Disabilities, University of North Carolina at Chapel Hill, United States of America*
[c] *Biomedical Imaging Research Institute (BIRI), Department of Biomedical Sciences and Imaging, Cedars-Sinai Medical Center, United States of America*
[d] *Department of Computer Science, University of North Carolina at Chapel Hill, United States of America*

ARTICLE INFO

Keywords:
Structural connectome
Functional connectome
Structure-function coupling
Graph convolutional neural network

ABSTRACT

There is strong evidence that the functional connectome is highly related to the white matter connectome in older children and adults, though little is known about structure-function relationships in early childhood. We investigated the development of cortical structure-function coupling in children longitudinally scanned at 1, 2, 4, and 6 years of age (N = 360) and in a comparison sample of adults (N = 89). We also applied a novel graph convolutional neural network-based deep learning model with a new loss function to better capture inter-subject heterogeneity and predict an individual's functional connectivity from the corresponding structural connectivity. We found regional patterns of structure-function coupling in early childhood that were consistent with adult patterns. In addition, our deep learning model improved the prediction of individual functional connectivity from its structural counterpart compared to existing models.

1. Introduction

The recent advances in neuroimaging techniques have enabled *in vivo* investigation of the human brain (Ciarrusta et al., 2022). Diffusion magnetic resonance imaging (dMRI) characterizes tissue microstructure and structural pathways (Johansen-Berg and Behrens, 2013), allowing the computation of anatomical brain networks or structural connectomes. Functional MRI (fMRI) captures physiologically co-activating brain networks or functional connectome. A structural connectivity (SC) matrix is derived from the streamline counts connecting a pair of brain regions by the diffusion tractography algorithm. On the other hand, functional connectivity (FC) matrix is computed by Pearson's correlation coefficients of time series fMRI signals of a pair of brain regions, representing the patterns of interaction between neuronal populations (Honey et al., 2009). There has been growing interest in understanding how structural and functional connectomes are related in individuals, and how they develop over time. While studies have related SC and FC in multimodal datasets, few have sought to study their associations developmentally with a focus on individual prediction.

The relationship between SC and FC is typically investigated using group-averaged measures. Studies showed significant correlations ($r^2 = 0.62$; (Hagmann et al., 2008) and $r^2 = 0.49$; (Honey et al., 2009)) between group-averaged SC and FC. The relationship between structure and function is also defined as S–F coupling which is computed as rank correlation between regional profiles of SC and FC of each individual and there is moderate correspondence between structure and function in terms of coupling based individual-level FC and SC (Honey et al., 2009; Baum et al., 2020). In addition, both structural and functional participation coefficients, a graph measure of how a node's connections are distributed among different sub-networks (Guimera and Amaral, 2005), are significantly associated with the variability in S–F coupling (Baum et al., 2020).

Although functional connections are shaped by physical connections, strong functional connections can exist between brain regions that are not directly connected by anatomical connections, which suggests that functional interactions between brain regions are determined by both direct and indirect connections (Li et al., 2021). This motivates the recent research studies more focused on predicting individual-level FC using deep learning models (Sarwar et al., 2021; Neudorf et al., 2022; Li et al., 2021). In Sarwar et al. (2021), the authors developed a deep learning framework to predict function from structure and demonstrated improved prediction performance compared to biophysical models. A graph neural network-based prediction model has also been proposed to predict FC as well as graph centrality measures (Neudorf et al., 2022). Their model is based on the Graph Nets (Battaglia et al., 2018) by learning node-level and edge-level

---

[*] Corresponding author.
E-mail address: yoonmi_hong@med.unc.edu (Y. Hong).

https://doi.org/10.1016/j.dcn.2023.101314
Received 13 June 2023; Received in revised form 27 September 2023; Accepted 12 October 2023

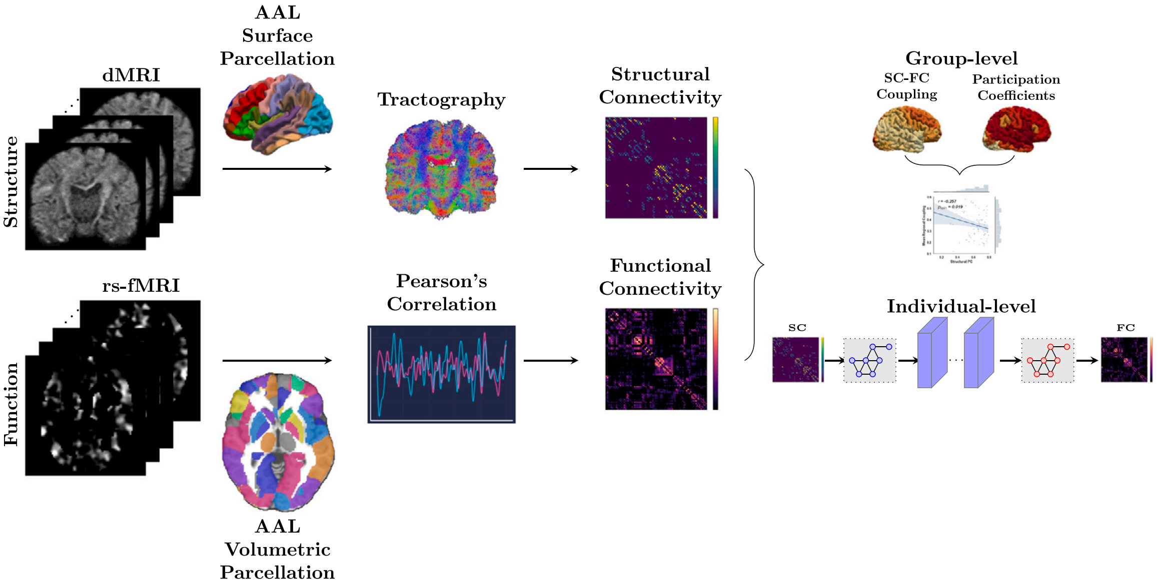

Fig. 1. Schematic overview Structural connectivity (SC) and functional connectivity (FC) matrices were generated from dMRI and rs-fMRI data, respectively. Relationships between structure and function were investigated by computing S–F coupling and participation coefficients from regional profile vectors of the connectivity matrices. Group-averaged regional coupling and participation coefficients were visualized, and their correlations were investigated. For individual-level analysis, each individual's FC was predicted from its SC using our proposed deep learning prediction model.

representations. In Li et al. (2021), the authors predicted FC from SC using a graph representation learning framework. On the other hand, individual SC was generated from FC using a multiple graph convolutional neural networks (GCN) based model (Zhang et al., 2022). These previous works were evaluated using healthy adults from the Human Connectome Project (HCP) database (Van Essen et al., 2013).

It is generally assumed that the structural connections are reflected in the corresponding functional connections (Passingham et al., 2002) and that the FC is constrained or determined in part by the white matter (WM) connectome in adults and older children. However, little is known about their relationship in early childhood when these connectomes are developing. The first years of life are characterized by rapid development of gray and white matter (Dubois et al., 2014; Gilmore et al., 2018). While major white matter tracts are in place by birth, microstructural maturation of these tracts proceeds rapidly in the first year or so of life, and more gradually thereafter (Ouyang et al., 2019; Sadeghi et al., 2013; Geng et al., 2012; Stephens et al., 2020). Studies also indicate that major aspects of the WM connectome are in place by birth (Huang et al., 2015; Bagonis et al., 2022) and even in 30 weeks old premature infants (Ball et al., 2014). In contrast, FC develops more slowly in early childhood, with sensorimotor network connections fairly mature by birth, and higher order networks maturing in the first few years of life (Gao et al., 2017; Smyser et al., 2011; Gao et al., 2015).

The first goal of this paper is to quantify the relationship between SC and FC in terms of S–F coupling and participation coefficients in early childhood. The second goal is to predict individual FC from SC using a GCN-based deep learning by learning a non-linear mapping. We hypothesized that S–F coupling would be apparent in early childhood and that patterns of S–F coupling would be adult-like. We also hypothesized that S–F coupling would be significantly related to the structural and functional participation coefficients. Finally, we hypothesized that individual FC could be predicted from the SC, specifically that SC at early ages could predict FC at later ages. The schema of the current study and the methods are illustrated in Fig. 1. We generated SC and FC for each subject in a longitudinal study with samples at 1, 2, 4, and 6 years of age.

2. Materials and methods

2.1. Datasets

Multi-modal neuroimaging data from the University of North Carolina (UNC) Early Brain Development Study (EBDS) was used for this study. The EBDS cohort consists of singletons, twins, and the high-risk offspring of mothers with schizophrenia or bipolar illness. Mothers were enrolled during pregnancy and the children were followed longitudinally with structural, diffusion weighted, and resting state fMRI after birth. For this analysis, subjects with scans at 1, 2, 4, and/or 6 years were included. One twin per twin pair was included, where twin A was selected if both twins had usable scans. Children were excluded if they had an abnormality on MRI or a major medical or surgical illness, including head injury or seizure disorder. Subjects were initially scanned with a Siemens 3T Allegra scanner, which was later replaced with a Siemens 3T Tim Trio (see Table 1). A total of 519 scans from 360 subjects were included.

In addition to EBDS dataset, a supplementary adult dataset of 89 subjects from the Human Connectome Project (HCP) (Van Essen et al., 2013) was used for the validation of our method. We used the minimally preprocessed HCP dataset of 100 unrelated subjects, and 89 subjects (41 male) with various ages (22–36 years) were included in this paper after imaging quality control of SC and FC. More details on imaging acquisition and preprocessing pipelines of HCP dataset can be found in Van Essen et al. (2013). In the remaining subsections below, we focus on the EBDS dataset, unless noted otherwise. It is noteworthy that this HCP dataset is of limited applicability as a validation dataset since the connectome generation and age distribution is different than in the pediatric EBDS population.

2.1.1. Image acquisition

Structural T1w images on the Siemens Allegra scanner were acquired using a three-dimensional magnetization-prepared rapid acquisition gradient-echo (MPRAGE) sequence: TR = 1880–1900 ms, TE = 4.38 ms, flip angle = 7°, voxel size = $1\times1\times1$ mm^3. T1w images on the Siemens Tim Trio scanner were acquired using a lower echo time: TR = 1860–1900 ms, TE = 3.74 ms, flip angle = 7°, voxel size = $1\times1\times1$ mm^3. T2w images on the Allegra scanner were collected using a dual echo

Table 1
Participant demographic and scan information.

	Overall Cohort (N=360)			
	Mean (SD)			
Gestational age at birth (days)	261.73 (18.62)			
Birth weight (g)	2860.88 (701.27)			
	n (%)			
Sex, male	188 (52.22%)			
Twin	180 (50%)			
Non High-risk Singleton	133 (37%)			
High-risk Singleton[a]	47 (13%)			
	1 year N=161	2 year N=135	4 year N=88	6 year N=135
	Mean (SD)	Mean (SD)	Mean (SD)	Mean (SD)
Age at scan (months)	13.03 (0.99)	25.06 (0.99)	48.87 (1.03)	73.05 (1.55)
Number of excluded gradients	3.14 (2.99)	2.61 (2.78)	5.88 (4.39)	4.44 (3.46)
Mean frame-wise displacement (mm)	0.09 (0.03)	0.10 (0.03)	0.12 (0.03)	0.12 (0.03)
	N(%)	*N*(%)	*N*(%)	*N*(%)
Allegra	110 (68%)	81 (60%)	6 (7%)	24 (18%)
Tim Trio	51 (32%)	54 (40%)	82 (93%)	111 (82%)

[a] Maternal diagnosis: Schizophrenia (13), Schizoaffective disorder (4), Psychosis NOS (2), Bipolar (9), Mood disorder NOS (11), other/unable to determine (8); NOS: not otherwise specified.

sequence: TR = 7380–7590 ms, TE1 = 20 ms, TE2 = 119 ms, flip angle = 150°, voxel size = $1.25\times1.25\times1.95$ mm^3. T2w images on the Tim Trio scanner were collected using a 3DT2 SPACE protocol: TR = 3200 ms, TE = 406–497 ms, flip angle = 120°, voxel size = $1\times1\times1$ mm^3.

Diffusion weighted images (DWIs) were acquired in both scanners with the same protocol employing 42 unique gradient directions, uniformly arranged across the sphere, with a b-value of 1000 s/mm^2 in addition to seven $b = 0$ images. The following acquisition parameters were used: twice refocused spin echo, TR = 7680 ms, TE = 82 ms, flip angle = 90°, voxel size = $2\times2\times2$ mm^3.

Functional images were acquired in both scanners using a T2*-weighted echo planar imaging (EPI) sequence: TR = 2000 ms, TE = 32 ms, 33 slices, voxel size = $4\times4\times4$ mm^3, 150 volumes. For rs-fMRI, all 1-, and 2-year-old subjects were in a natural sleep state, while all 4- and 6-year-old subjects were awake during the imaging session; all 4-year-olds watched cartoons and 6-year-olds watched either an animated movie (99 subjects) or a fixation cross (36 subjects).

2.1.2. *Structural image processing*

T1-weighted images were corrected for intensity inhomogeneity and rigidly registered into pediatric Montreal Neurological Institute (MNI) template space. Then, the skull was extracted using the majority voting approach of several deformably registered atlases as well as masks from the FSL Brain Extraction Tool (Smith, 2002). WM surfaces were reconstructed via a CIVET v2.1 workflow adapted for pediatric data using an age-specific atlas (Kim et al., 2005). This workflow also provided a surface-based labeling with the Automated Anatomical Labeling (AAL) 78 cortical brain regions. Note that the white matter surface is the boundary between gray matter and white matter. The AAL template subdivides gray matter at the boundary of white matter.

Subcortical structures (hippocampus, amygdala, caudate, putamen, pallidum, and thalamus) were segmented using a multi-atlas based approach (MultiSeg v.2.2.1) (Pham et al., 2019) with 32 templates aged 1–6 years of age. Subcortical surfaces were reconstructed via the SPHARM-PDM framework (Besson et al., 2014; Piot et al., 2022) leading to a uniformly sampled surfaces with 1002 vertices for each subcortical structure. More detailed parameters for subcortical surface processing can be found in Table S1 in the supplementary material. By combining 78 WM surfaces and 12 subcortical surfaces, we created an AAL-equivalent 90 surface parcellation.

Quality assessment procedures for the raw MRI data, intermediate processing steps, as well as the generated cortical and subcortical labels were performed for all datasets.

2.2. *Structural connectome processing*

2.2.1. *dMRI data processing*

DTIPrep (Oguz et al., 2014) was used to correct for eddy current and motion artifacts, and to remove DWI volumes that had significant slice-wise brightness and motion-related interlace artifact. Following DTIPrep, the remaining corrected DWI volumes were visually inspected, and additional volumes were dropped if they contained significant residual artifacts. DWIs with less than 50% of the original number of volumes remaining after this preprocessing procedure were fully excluded. The average number of excluded gradients at each year is shown in Table 1.

We upsampled DWIs to $1\times1\times1$ mm^3 using a cubic Catmull–Roll kernel. Rigidly co-aligned T1w and T2w images were registered to the same subject's DWI space. First, a rigid transform was computed aligning a subject's T2w image to the average of its baseline ($b = 0$) images (BRAINS-Fit (Johnson et al., 2007)). Using the rigid transform as initialization, a deformable symmetric diffeomorphic co-registration was calculated using advanced normalization tools (ANTs) (Avants et al., 2008) with 2 cross-correlation terms. The first term matched the T1w image to the tensor-derived fractional anisotropy (FA) map; the second cross-correlation term, at double weight, matched the T2w image to the average of the baseline images. Both the T1w image and the structural surface were brought into DWI space by applying the rigid and non-linear transforms. Vertex wise AAL 90 labels are then used to define seed regions for the structural connectivity computation. Visual inspection of the WM and subcortical surfaces overlaid on the average baseline image was performed using 3D Slicer to ensure accuracy of the registration by checking the surface's alignment with the white–gray matter boundary.

2.2.2. *Structural connectivity matrices*

Bayesian estimation of diffusion parameters modeling the diffusion coefficient as a Gamma distribution was computed with FSL's bedpostx (Jbabdi et al., 2012) to allow for multiple orientations and crossing fibers prior to tractography. A maximum of 2 crossing fibers were modeled at each voxel. Using FSL's probtrackx2 (Behrens et al., 2007), each labeled vertex on the WM surface or subcortical surfaces was used as a seed to initiate tractography (per scan, WM surface: 320,000 seeds, subcortical surfaces: 12,000 seeds). The number of streamlines per seed was set to 1000, and a step length of 0.75 mm and a seed sphere sampling size of 0.5 mm were used. Raw streamline counts were recorded in 90 × 90 connectivity matrices. Then, connectome matrices were corrected such that the spatial seed sampling across subcortical and WM surfaces are matched. This correction ensures that, in average, all surfaces lead to an equally spatially sampled connectome. Then we symmetrize and normalize the matrices so that the summation of the lower triangular parts equals to 1.

2.3. Functional connectome processing

2.3.1. fMRI data processing

Functional imaging data were preprocessed using FMRIB's Software Library (FSL) (Smith et al., 2004) and analysis of functional neuroimages (AFNI) (Cox, 1996). Preprocessing included rigid-body motion correction, registration, bandpass filtering (0.01–0.08 Hz), scrubbing, nuisance signal regression, and global signal regression. For motion correction, the first frame of functional image served as the target image. Frame-wise displacement (FD) was estimated from the 6 motion parameters (displacements and rotations). The full functional datasets were aligned to the template image using per-volume transformations; rigid-body within functional + nonlinear functional-to-anatomical + nonlinear anatomical-to-standard. Both nonlinear registrations used ANTs (Avants et al., 2008). The age-specific template (Shi et al., 2011) served as the target space. Each subject was visually checked to ensure successful registration. Data scrubbing was performed as an additional motion correction step other than the standard rigid-body motion correction procedures; volumes with FD higher than 0.3 mm were removed ("scrubbed") from the data; if fewer than three volumes remained between the scrubbed volumes, then these volumes were also removed (Power et al., 2012). Participants with < 90 volumes remaining (3 min) were excluded from further analysis. The nuisance signal regression model included 32 parameters (32P); 8 regressors corresponding to white matter and cerebral spinal fluid signals, as well as the 6 motion estimates, plus their derivative, quadratic, and squared derivative terms (Power et al., 2014). The data were warped to standard space, spatially smoothed using a Gaussian kernel of 6-mm full width at half maximum, and truncated to 90 volumes. The 2-year template (Shi et al., 2011) served as the final target for spatial registration; rs-fMRI data across all ages were aligned to the same 2-year template space for subsequent analyses. Lastly, global signal regression was performed to regress out the mean gray matter signal from the data.

2.3.2. Functional connectivity matrices

After preprocessing, the 90 × 90 functional connectivity matrices were obtained based on the infant 2-year AAL atlas (Shi et al., 2011). Specifically, the average fMRI time series for each AAL region were calculated by averaging time series across all voxels within the AAL region. The pair-wise correlation between one region and the other was calculated across all 90 AAL regions to form the 90 × 90 functional connectivity matrix for each subject. The correlation values were Fisher-Z transformed for subsequent statistical analyses. In order to match the sparsity of the structural matrices, the functional connectivity matrices were thresholded using different strategies and levels. Specifically, there were two strategies: individual-level thresholding, which used the correlation p values for thresholding individually; and group-level thresholding, which used the group-level t-test p values for thresholding at group-level. For each strategy, there were three different levels of significance: $p < .05$, FDR-corrected (Benjamini and Hochberg, 1995); $p < .001$, uncorrected; $p < .01$, uncorrected. Since global signal regression was performed during preprocessing, all thresholded functional connectivity matrices were further processed to have only positive values: for individual-level matrices, negative values were directly put to zeros; for group-level matrices, the cells with negative t values in group-level t-tests were firstly put to zeros so that the topology across subjects in the same age group is consistent, followed by another step that the negative values were also put to zeros individually, which causes the only differences in group-level topology.

2.4. Human connectome project processing

Details about acquisition parameters and pre-processing for the Human Connectome Project (HCP) dataset can be found in Glasser et al. (2013), Van Essen et al. (2013). All DWI volumes were visually inspected, and if significant artifacts were visible, the entire DWI acquisition was excluded from analysis. The co-registered T1w and T2w images in MNI space were registered to the same subject's DWI in native space following similar registration steps as for the EBDS data. FreeSurfer (Dale et al., 1999) was used to reconstruct cortical surfaces. This reconstruction used the FreeSurfer 5.3.0-HCP pipeline and the multimodal surface matching (MSM-All) algorithm (Glasser et al., 2016) resulting in cortical surfaces with 164K vertices per hemisphere in MNI space. We applied an AAL labeling map for the FreeSurfer surfaces via the majority voting using the cortical surfaces from 25 subjects. The T1w images and WM surfaces were brought into DWI space following the same protocol as for the EBDS data. We performed a visual inspection of the transformed WM surface overlaid on both a B0 image and the T1w image in DWI space for each subject.

Structural connectivity matrices were generated in the same manner as for the EBDS data except a maximum of 3 crossing fibers were modeled at each voxel (due to the higher number of acquired diffusion gradients in the HCP data), and subcortical structures were not included. Streamline counts were recorded in 78 × 78 connectivity matrices.

The preprocessing of rs-fMRI is consistent with the processing for the EBDS data except for the different template (MNI adult template) and the truncation to 1500 volumes.

2.5. Structure-function coupling

The combination of dMRI and rs-fMRI connectivity data allows us to quantify how the brain's structural connectome (SC) provides support for the spontaneous fluctuation in neural activity as captured by the functional connectome (FC). As a first measure, we employ Structure-Function coupling, which is measured as the Spearman's rank correlations between regional profiles of SC and FC matrices (Baum et al., 2020). We generated 78 × 78 SC matrix associated with cortical regions from tractography based on the AAL 78 cortical region parcellation. FC matrix with 78 × 78 was extracted from 90 × 90 matrix by neglecting the elements corresponding to subcortical regions. Note that only 78 cortical regions were used for S–F coupling analysis to facilitate comparison with the previous results from different age cohorts (Honey et al., 2009; Baum et al., 2020). The coupling coefficient was computed by Spearman's rank correlation between the regional structural and functional profiles.

Secondly, we also use the participation coefficient (PC), which is a graph measure that finely characterizes hub and non-hub nodes (Guimera and Amaral, 2005). The participation coefficient P_i for a node i is defined as

$$P_i = 1 - \sum_{s=1}^{N_M} \left(\frac{\kappa_{i,s}}{k_i} \right)^2, \tag{1}$$

where $\kappa_{i,s}$ is the number of edges of the node i to other nodes in the module s, k_i is the degree of node i, and N_M is the number of modules. In this paper, we used 8 different groups of networks to identify the module (Yeo et al., 2011). The association between structure-function coupling and functional specialization was assessed by the PC (Baum et al., 2020). The nodes with higher PC exhibit diverse and integrated inter-modular connectivity, whereas the nodes with lower PC exhibit locally segregated connectivity within the module (Baum et al., 2020).

2.6. Statistical analysis

As our datasets were scanned at two different scanners, we applied ComBat (Fortin et al., 2018) to harmonize the S–F coupling and participation coefficients. For S–F coupling, we used sex, high risk status, gestational age at birth, the number of QC'ed gradients, and the frame-wise displacement as ComBat covariates that need to be preserved. The rs-fMRI scan protocol (movie vs. fixation) is considered as an additional covariate at age 6. For structural PC, sex, high-risk status, gestational age at birth, and the number of QC'ed gradients were used as covariates. For functional PC, sex, high-risk status, gestational age at birth, and the framewise displacement, as well as rs-fMRI scan type for at age 6, were used as covariates.

A Pearson correlation analysis at each age was employed to identify the covariates with which S–F coupling, structural PC, and functional PC were correlated by each node. Covariates with significant correlations for more than 5% of the nodes were included in the model.

For each of the connectome measures (S–F coupling, structural PC, and functional PC), we consider age connectome measurements as repeated measures to account for within-subject correlations over time. For tracing the longitudinal behavior of S–F coupling, least-square (LS) means were computed using linear mixed models (LMM) with age, gestational age at birth, sex, number of QC'ed gradients, frame-wise displacement and the interactions age with number of QC'ed gradients and age with frame-wise displacement as predictors. For structural PC, LS means were computed using LMM with age, gestational age at birth, sex, number of QC'ed gradients and the interaction age with number of QC'ed gradients as predictors. For functional PC, LS means were computed using LMM with age, gestational age at birth, sex, frame-wise displacement and the interaction age with frame-wise displacement as predictors. The temporal power covariance structure was selected for all LMM models. Bayesian Information Criteria was used to identify the predictor terms and the covariance structure that yield the best-fit LMM model. As there were two rs-fMRI scan protocols (movie vs. fixation) only at age 6, the effect of the rs-fMRI scan protocol on the connectome measures (S–F coupling and functional PC) in excess to the other covariates was weight-averaged over the age 6 cohort prior to the calculation of LS means via LMM.

For HCP dataset, LS means of S–F coupling and functional PC were computed using linear models (LM) with sex and frame-wise displacement as predictors, and LS means of structural PC were computed using linear models (LM) with sex as predictor.

The null hypotheses that there is no difference in between the measures at two ages were tested using those linear mixed models. The *p*-values were adjusted using an FDR correction to account for multiple comparisons across the 78 cortical nodes.

2.7. Prediction model

For individual prediction, we employed a GCN based prediction model for predicting individual-level FC from SC in early childhood. Spectral graph convolutional neural networks were introduced for a convolutional operation on graph structured data. ChebNet utilizes multi-hop neighborhood information by approximating the coefficients of Chebyshev polynomial of the graph Laplacian (Defferrard et al., 2016). Note that the graph spectral filters generated by Kth order Chebyshev polynomial can be efficiently computed using recurrence relation and are exactly K-hop localized. Kipf and Welling (2016) proposed a simplified ChebNet by renormalizing the adjacency matrix with $K = 1$, thereby operating on only 1-hop neighborhood. To leverage the information from indirect connections as well as direct connections, we adopt ChebNet with $K = 5$ in this paper. Multi-task learning or joint learning has been introduced in many medical imaging applications, where the features of multiple output tasks such as disease classification and clinical score regression are highly correlated (Liu et al., 2018). In this paper, we simultaneously predict the target FC, the subject's age at scan time, and the employed scanner type from the input SC. As discussed in Li et al. (2021), this multi-task learning framework can provide the right balance between preserving the inter-subject heterogeneity and estimating population patterns. We further employed a Generative Adversarial Network (GAN) to generate more realistic outputs as it has been shown to improve perceptual quality in many image-based prediction tasks (Goodfellow et al., 2014). In this study, a GCN-based generator generates the target FC while a discriminator is trained to distinguish real from fake FCs.

We propose a machine learning framework for individual-level prediction from the structural connectome to the functional connectome. Our aim is to learn a non-linear mapping, which predicts the individual FC from its SC, based on graph convolutional neural network (GCN). Fig. 2 shows the overview of the GCN based framework. Unlike dense neural networks applied to a flattened vector of lower triangular part of connectivity matrices (Sarwar et al., 2021), our framework takes the whole connectivity matrix as a weighted adjacency matrix into the GCN architecture to generate the FC, preserving the brain network structure. We found that this GCN based architecture has significantly less number of learnable parameters compared to dense networks, which can avoid overfitting the high number of parameters in deep learning models to the comparatively low number of samples. Moreover, while in Sarwar et al. (2021) the SC matrix is resampled to a Gaussian distribution and rescaled in order to normalize it for the deep neural network training, our GCN based model does not require Gaussian resampling of the connectivity matrices. Such Gaussian resampling can enhance the noise in the connectivity data, and thus it is preferable to avoid it, if possible.

Our prediction framework has a generator and a discriminator so that the network is trained in an adversarial way for better prediction performance. The generator consists of three GCN layers, where the graph convolutional operation employs a Chebyshev polynomial approximation of the graph Laplacian.

Let A be the weighted graph adjacency matrix and N be the number of nodes in the graph. Then graph Laplacian operator L can be defined as $L = I_{N\times N} - D^{-1/2}AD^{-1/2}$ with $I_{N\times N}$ being the identity matrix and D being the diagonal degree matrix $D_{ii} = \sum_j A_{ij}$. Let $\mathbf{H}^{(l)} \in \mathbb{R}^{N\times d^{(l)}}$ be lth layer features, where $d^{(l)}$ is the number of features at lth layer. The output features in GCN layers are updated as

$$\mathbf{H}^{(l+1)} = \xi\Big(\sum_{k=0}^{K} T_k(\tilde{L})\mathbf{H}^{(l)}\mathbf{W}_k^{(l)}\Big), \tag{2}$$

where ξ is a non-linear activation function and $\mathbf{W}_k^{(l)} \in \mathbb{R}^{d^{(l)}\times d^{(l+1)}}$ is the matrix of learnable parameters at lth layer, representing kth order Chebyshev polynomial coefficients. Here, $T_k(\tilde{L})$ is the kth order Chebyshev polynomial evaluated on the scaled graph Laplacian $\tilde{L} := 2L/\lambda_{\max} - I$ with $\lambda_{\max}$ being the maximal eigenvalue of L. Note that the spectral filters learned as Kth order Chebyshev polynomial coefficients are exactly K-localized and can be computed recursively (Defferrard et al., 2016).

While a generator creates the target FC matrix from SC, a discriminator differentiates the generated connectivity matrices from the ground-truth samples. The discriminator consists of two GCN layers followed by a series of fully connected layers, where the output is a classification probability for real and fake samples. The input features are set as the identity matrix for both generator and discriminator. The adjacency matrices for the GCN layers in the generator and discriminator are normalized SC matrices and real/fake FC matrices, respectively.

We designed a loss function for the generator, consisting of five different terms: mean-squared loss, correlation loss, paired Siamese loss, regularization loss, and adversarial loss. Let $\mathbf{x}_i$ be an input SC, $\mathbf{y}_i$ ground-truth FC, and $f(\mathbf{x}_i)$ predicted FC. Then the generator loss function is defined as

$$\mathcal{L}_G = \mathcal{L}_{\text{MSE}} + \lambda_{\text{corr}}\mathcal{L}_{\text{corr}} + \lambda_{\text{siamese}}\mathcal{L}_{\text{siamese}} + \lambda_{\text{reg}}\mathcal{L}_{\text{reg}} + \lambda_{\text{ADV}}\mathcal{L}_{\text{ADV}}, \tag{3}$$

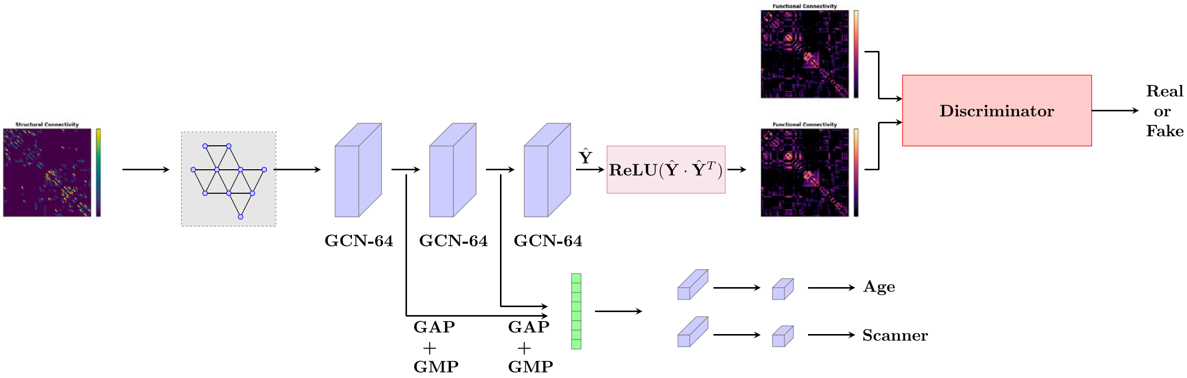

Fig. 2. Overview of the prediction model based on graph convolutional neural network. Our framework consists of a generator and a discriminator, where a generator predicts a target FC and a discriminator classifies real FC and generated FC. GCN-n denotes GCN layer with n output features. To ensure the symmetry and non-negativity of FC, the output of the last layer is multiplied by its transposed matrix, followed by ReLU activation. We concatenate the latent feature vectors from global average pooling (GAP) and global max pooling (GMP), and apply multi-layer perceptrons for age and scanner classification tasks.

where

$$\mathcal{L}_{\mathrm{MSE}} = \sum_i |\mathbf{y}_i - f(\mathbf{x}_i)|^2, \tag{4}$$

$$\mathcal{L}_{\mathrm{corr}} = \sum_i [1 - r(\mathbf{y}_i, f(\mathbf{x}_i))], \tag{5}$$

$$\mathcal{L}_{\mathrm{siamese}} = \sum_{i \neq j} \left[r(\mathbf{y}_i, \mathbf{y}_j) - r(f(\mathbf{x}_i), f(\mathbf{x}_j)) \right]^2, \tag{6}$$

$$\mathcal{L}_{\mathrm{reg}} = \sum_i \left[r(\mathbf{y}_i, \bar{\mathbf{y}}) - r(f(\mathbf{x}_i), \bar{\mathbf{y}}) \right]^2, \tag{7}$$

$$\mathcal{L}_{\mathrm{ADV}} = \mathcal{L}_{\mathrm{BCE}}(D(f(\mathbf{x}_i)), 1), \tag{8}$$

where r is a Pearson's correlation function and $\mathcal{L}_{\mathrm{BCE}}$ is the binary cross-entropy function defined as

$$\mathcal{L}_{\mathrm{BCE}}(\hat{\mathbf{z}}, \mathbf{z}) = -\sum_i [z_i \log(\hat{z}_i) + (1 - z_i) \log(1 - \hat{z}_i)]. \tag{9}$$

The weights λ_{corr}, $\lambda_{\mathrm{siamese}}$, λ_{reg}, and λ_{ADV} in Eq. (3) control the contributions of different loss terms.

Inspired by the regularization term defined in Sarwar et al. (2021), we added a paired inter-subject difference loss $\mathcal{L}_{\mathrm{Siamese}}$ to ensure that the correlation of the predicted FCs across different subjects are comparable to the correlation of ground-truth connectivity. Additionally, we compared the difference between the predicted and real FC with the group-averaged FC $\bar{\mathbf{y}}$ to regularize inter-subject variation. Both of these regularization terms help to retain inter-subject heterogeneity, avoiding the case that the prediction converges to the group-averaged FC. We performed an ablation study in which the error of inter-subject correlation (ISC) is defined as follows. For each subject i, let $\mathbf{y}_i$ and $\hat{\mathbf{y}}_i$ be ground-truth FC and predicted FC, respectively. The error of ISC was defined as the difference between the mean ISC of the ground-truth and the mean ISC of the predictions:

$$\left| \frac{1}{N-1} \sum_{j \neq i} r(\mathbf{y}_i, \mathbf{y}_j) - \frac{1}{N-1} \sum_{j \neq i} r(\hat{\mathbf{y}}_i, \hat{\mathbf{y}}_j) \right|. \tag{10}$$

The discriminator loss function is defined as binary cross-entropy loss:

$$\mathcal{L}_D = \mathcal{L}_{\mathrm{BCE}}(D(\mathbf{y}), 1) + \mathcal{L}_{\mathrm{BCE}}(D(f(\mathbf{x}), 0)), \tag{11}$$

where the discriminator outputs high probability for the real sample $\mathbf{y}$ and low probability for the generated FC $f(\mathbf{x})$.

In addition to the reconstruction of FC, our model is designed to predict the scanner and age of the connectivity to fully utilize the available subject information. To reduce the effects of different scanners and different ages, we added two different classification branches on top of the FC prediction. We applied multi-layer perceptrons to the flattened vector, which is obtained by concatenating a global average pooling layer and a global max pooling layer on the latent representation. Each classification branch predicts the scanner and age at scan, independently. The numbers of output nodes for scanner and age prediction are 2 and 4, respectively. We utilized the ordinal regression loss for the age prediction, since the age classes are finite ordered categories (Cheng et al., 2008). As in Cheng et al. (2008), the target vector for the ordinal regression was encoded as $(1, 1, \ldots, 0)$ where the first k elements are 1 and others 0, for the class k. In addition, instead of soft-max output for the traditional classification task, each output node was activated using the sigmoid function. We adopted a Mean Squared Error (MSE) loss for the age classification:

$$\mathcal{L}_{\mathrm{age}} = \sum_{t=1}^{T} |\alpha_t - \hat{\alpha}_t|^2, \tag{12}$$

where T is the total number of different ages in this study, α_t is the ground-truth target vector $(1, 1, \ldots, 0)$ where the first t elements are 1 and others 0. $\hat{\alpha}_t$ is the output probability at node t.

For scanner classification, as the scanner distribution is highly imbalanced especially at age 4, the focal loss (Lin et al., 2017) with the focusing parameter $\gamma = 2$ was applied.

The final loss function for the training is defined as

$$\mathcal{L} = \mathcal{L}_G + \lambda_{\mathrm{age}} \mathcal{L}_{\mathrm{age}} + \lambda_{\mathrm{scan}} \mathcal{L}_{\mathrm{scan}}. \tag{13}$$

2.8. Implementation details

All statistical analysis was performed in SAS 9.4. Alpha = 0.05 level of significance was used for all significance testing, and a Benjamini–Hochberg false discovery rate correction was used for all nodal analyses of S–F coupling, structural PC, and functional PC. All statistical tests were two-sided, unless stated otherwise.

For individual-level prediction, we trained our model implemented in PyTorch 1.7.0. The initial learning rate was set to 0.001 and the ADAM optimizer was used. The learning rate was decayed using a learning rate scheduler by reducing the learning rate by a factor of 0.1 when the loss does not decrease for 10 consecutive epochs. The weights for the generator were set as follows: $\lambda_{\mathrm{ADV}} = 0.01$, $\lambda_{\mathrm{corr}} = 1.5$, $\lambda_{\mathrm{siamese}} = \lambda_{\mathrm{reg}} = 1.0$. The weights for classification tasks were set to 0.1 and 0.001 for λ_{age} and λ_{scan}, respectively. The total number of training epwas were 100, and the batch size was set to 1 since we aim for the training to be sensitive to individual variability. The source code is publicly available at https://github.com/yoonmihong/SCFC.

3. Results

We first visualize the average connectome for each age in Fig. 3. Group-averaged SC remains highly stable across the ages, while some

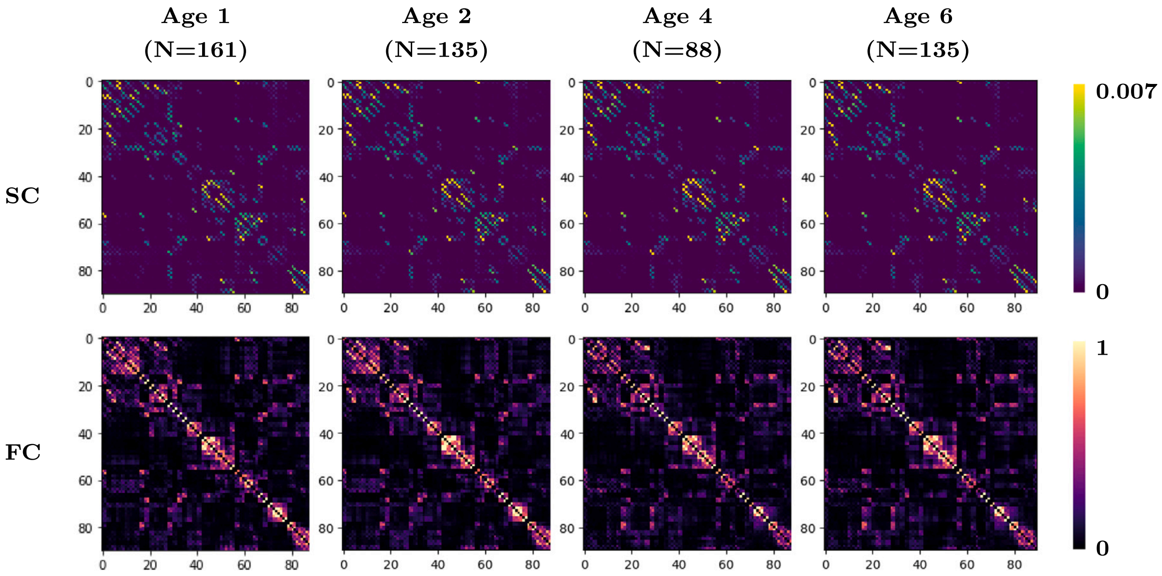

Fig. 3. Group-averaged structural connectivity (SC) and functional connectivity (FC) matrices at ages 1, 2, 4, and 6. Group-averaged SC matrices are highly stable across the ages, while FC matrices change across the ages, especially from age 2 to 4. Note that the scan paradigm was changed from sleep to movie-watching from age 2 to 4. Note that the display range of the colormap was set to be maximized for the visualization purposes.

of the connections in FC change from age 2 to 4, likely due to both brain development and partly the change of scan paradigm from sleep to movie-watching.

3.1. Structure-function cortical coupling

The first objective of this paper is to characterize how the white matter fiber architecture supports the spontaneous fluctuation in neural activity. S–F coupling was computed for each individual at each age: 1, 2, 4, and 6-years-old. We used group-level thresholded FC with $p < 0.01$ to compute its rank correlation with SC (Supplemental Table 3). The average regional S–F coupling at each age is shown in Fig. 4. Adult results from the HCP are included as a comparison. Regions with the highest S–F coupling ($n = 16$, top 20%) at age 6 years included mainly default mode (L&R Front Med Orb; L&R Ant Cingulum, R Precuneus, R Front Inf Oper, L Front Inf Orb) and visual (L&R Calcarine, R Cuneus, L&R Lingual) network regions, as well as somatomotor (R Paracentral Lobule), limbic (L Rectus, L Olfactory) and ventral attention (L Mid Cingulum) regions. Seven of these regions also had high S–F coupling at age 1, including default (L&R Front Med Orb; L&R Ant Cingulum), visual (L Calcarine, R Cuneus), and ventral attention (L Mid Cingulum) regions. At age 2, 10 of the 16 six year regions with the strongest S–F coupling were high S–F coupling regions. By age 4, all age 6 top S–F coupling regions were top S–F coupling regions.

While direct comparison is difficult due to difference in the EBDS and HCP cohorts, 7 of the top 16 regions with the strongest S–F coupling in adults were also high S–F coupling regions in 6 year olds, and 4 regions (L&R Ant Cingulum, L Mid Cingulum, L Calcarine) were among the strongest S–F regions in 1 year olds. This may indicate that while S–F coupling patterns continue to mature after age 6, some aspects of adult regional S–F coupling patterns are established in early childhood.

Age related changes in S–F coupling are presented in Fig. 5 and Supplemental Table 4. Between age 1 and 6 years, most cortical regions experience a significant decrease in S–F coupling ($n = 40$), while 19 regions had a significant increase, and 19 regions had no change. From 1–2 years, 42 regions had a significant decrease in S–F coupling, while only one region experienced a significant increase. In contrast, from age 2–4 years, 22 regions experienced a significant decrease in S–F coupling and 33 regions had a significant increase. Between the ages of 4 and 6 years, most regions had no change in S–F coupling ($n = 66$); 7 regions had a significant decrease and 5 had a significant increase (Supplemental Table 4).

From 1 to 6 years, the regional pattern of SC participation coefficient (PC) strength was relatively stable (Supplemental Table 5, Fig. 6), while that of the FC PC changed with age (Supplemental Table 6). The strength of S–F coupling is inversely related to the PC of the structural and functional connectome in older children and adolescents (Baum et al., 2020). We found that S–F coupling was significantly negatively related to structural PC at each age studied. In contrast, S–F coupling was significantly negatively related to the functional PC at only 1 and 2 years (Fig. 6). In the HCP adults, there were no significant relationships between S–F coupling and the structural or functional PC (Fig. S2).

3.2. Prediction of FC from the WM connectome

Using our machine learning approach, we were able to predict the FC from the SC with some accuracy. For each age, the mean Pearson coefficient for the predicted FC compared to the ground truth FC, was in the range of 0.7 (see Table 2 and Fig. S6 (b)), similar to that achieved in a previous study in adults (Sarwar et al., 2021). Representative individual prediction results and prediction correlations are shown in Fig. 7, demonstrating that our methods can predict FC which is close to the ground-truth FC with higher prediction correlation. It was also possible to predict the FC at age 6 from the SC at earlier ages, including the age 1, with similar accuracy using a longitudinal prediction model in which the input is SC at an earlier age and the output is FC at age 6. Since a subject can be scanned in a different scanner in this longitudinal prediction model, we trained the prediction model without scanner/age prediction branches. A representative prediction result generated from SC at age 1 is shown in Fig. S7, demonstrating that our model can predict individual FC from their SC at an earlier age. Quantitative results are summarized in Table 3, showing that our method can predict FC from SC at earlier ages with high prediction accuracy. It is also possible to predict the FC at age 6 from the FC at earlier ages, though the accuracy is significantly lower than that obtained with the SC (Table 3). In order to test whether the high-risk subjects affect the performance of the prediction model, we additionally trained the model by excluding high-risk offspring subjects. The quantitative results were summarized in Table S2 demonstrating that the model was generalized better with more subjects including the high-risk group.

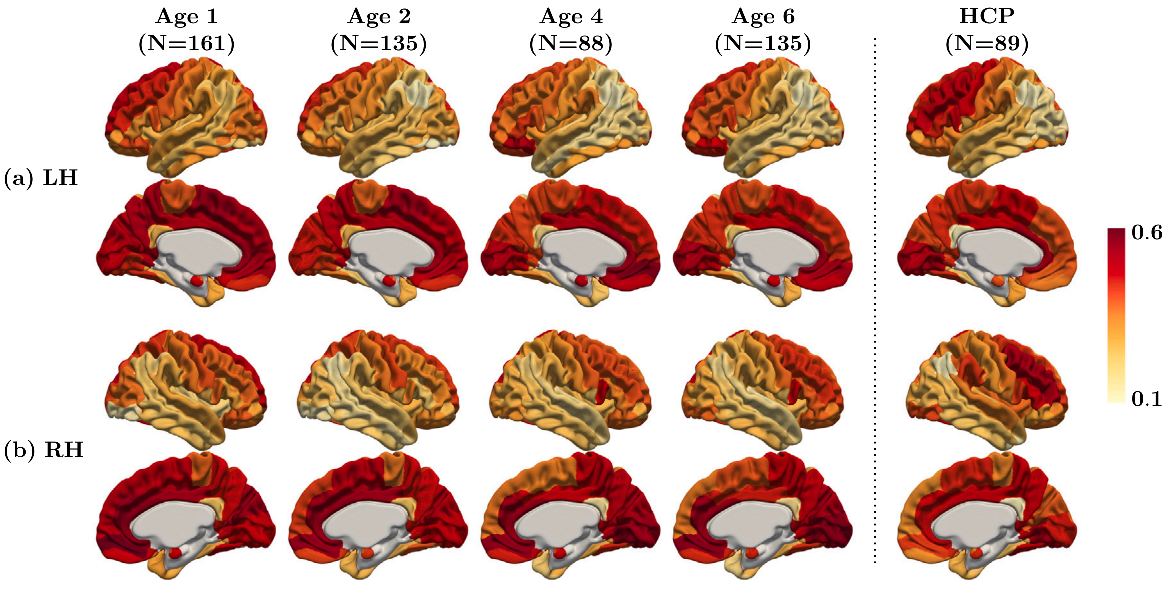

Fig. 4. Average regional structure-function coupling computed at ages 1, 2, 4, and 6 from EBDS and HCP dataset. Frontal lobes and medial parietal and occipital lobes showed relatively strong structure-function coupling, and lateral temporal and parietal regions showed relatively weaker coupling. Note that the scan paradigm was changed from sleep to movie-watching from age 2 to 4.

Table 2
Quantitative results for same-age prediction.

	MAE	Pearson’s coeff.
SC1 to FC1 (N=161)	0.075 ± 0.005	0.724 ± 0.032
SC2 to FC2 (N=135)	0.076 ± 0.006	0.718 ± 0.030
SC4 to FC4 (N=88)	0.071 ± 0.005	0.716 ± 0.031
SC6 to FC6 (N=135)	0.074 ± 0.006	0.720 ± 0.031

Table 3
Quantitative results for longitudinal prediction.

	MAE	Pearson’s coeff.
SC1 to FC6 (N=36)	$\mathbf{0.078 \pm 0.006}^{***}$	$\mathbf{0.714 \pm 0.035}^{*}$
FC1 to FC6 (N=36)	0.082 ± 0.005	0.700 ± 0.035
SC2 to FC6 (N=48)	$\mathbf{0.077 \pm 0.006}^{****}$	$\mathbf{0.709 \pm 0.033}^{*}$
FC2 to FC6 (N=48)	0.081 ± 0.006	0.696 ± 0.033
SC4 to FC6 (N=38)	$\mathbf{0.076 \pm 0.007}^{**}$	$\mathbf{0.717 \pm 0.049}$
FC4 to FC6 (N=38)	0.080 ± 0.005	0.704 ± 0.038

**** denotes $p \le 0.0001$, *** denotes $0.0001 < p \le 0.001$, ** denotes $0.001 < p \le 0.01$, and * denotes $0.01 < p \le 0.05$.

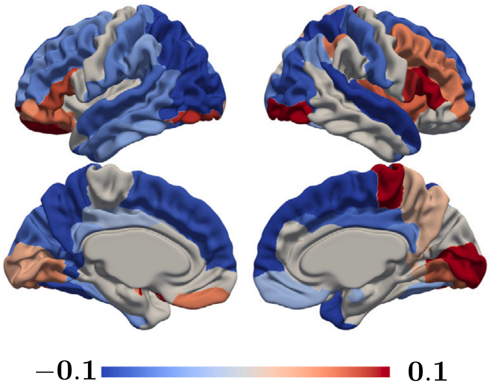

Fig. 5. Developmental changes of regional structure-function coupling LS means from age 1 to 6 (N=30). Between age 1 and 6 years, most cortical regions experience a significant decrease in S–F coupling ($n = 40$), while 19 regions had a significant increase, and 19 regions had no change.

3.3. Classification of age and scanner

We aim to utilize all available datasets, not training the prediction model at each age or scanner separately. To this end, we added two classification branches in addition to the reconstruction of FC. The classification results for scan ages and scanners are shown in Fig. 8. F1 scores for the age classification and the scanner classification are 0.75 and 0.94, respectively. Scanner classification accuracy was higher than the age classification accuracy due to the large number of samples for each class. Our model was able to distinguish different scanners from SC, and thus we did not apply ComBat to the input SC for data harmonization.

3.4. Ablation study

Our prediction model utilized SC as a weighted adjacency matrix in GCN layers. Normalization of SC such as Gaussian resampling in Sarwar et al. (2021) was not adopted as it highlights noisy connections and insufficiently represents the relative weights of the graph.

Our method is not sensitive to different hyperparameter settings except for λ_{corr}. As shown in Fig. 9, the results without adversarial loss or correlation loss were significantly decreased compared to the proposed methods with them. Note that the results without siamese loss or regularization loss slightly improve MAE and Pearson’s correlation. However, as in Fig. 9 and Fig. S8, their errors of inter-subject correlation (ISC) defined in Eq. (10) were larger than the proposed method. Overall, our proposed methods with all loss terms provide a reasonable balance between the prediction accuracy and inter-subject variability.

3.5. Sensitivity analysis

We performed a sensitivity analysis excluding the high-risk offspring. The numbers of typically developing subjects at ages 1, 2, 4, and 6 are 133, 112, 81, and 121, respectively. The average regional S–F coupling, age-related changes in S–F coupling, and the regional pattern of participation coefficients are shown in Figs. S3–S5 and Supplemental Tables S7-S10. We did not perform statistical analyses on the high-risk sample due to the small sample size. We found that after excluding high-risk children, the S–F coupling results and participation coefficients were very similar.

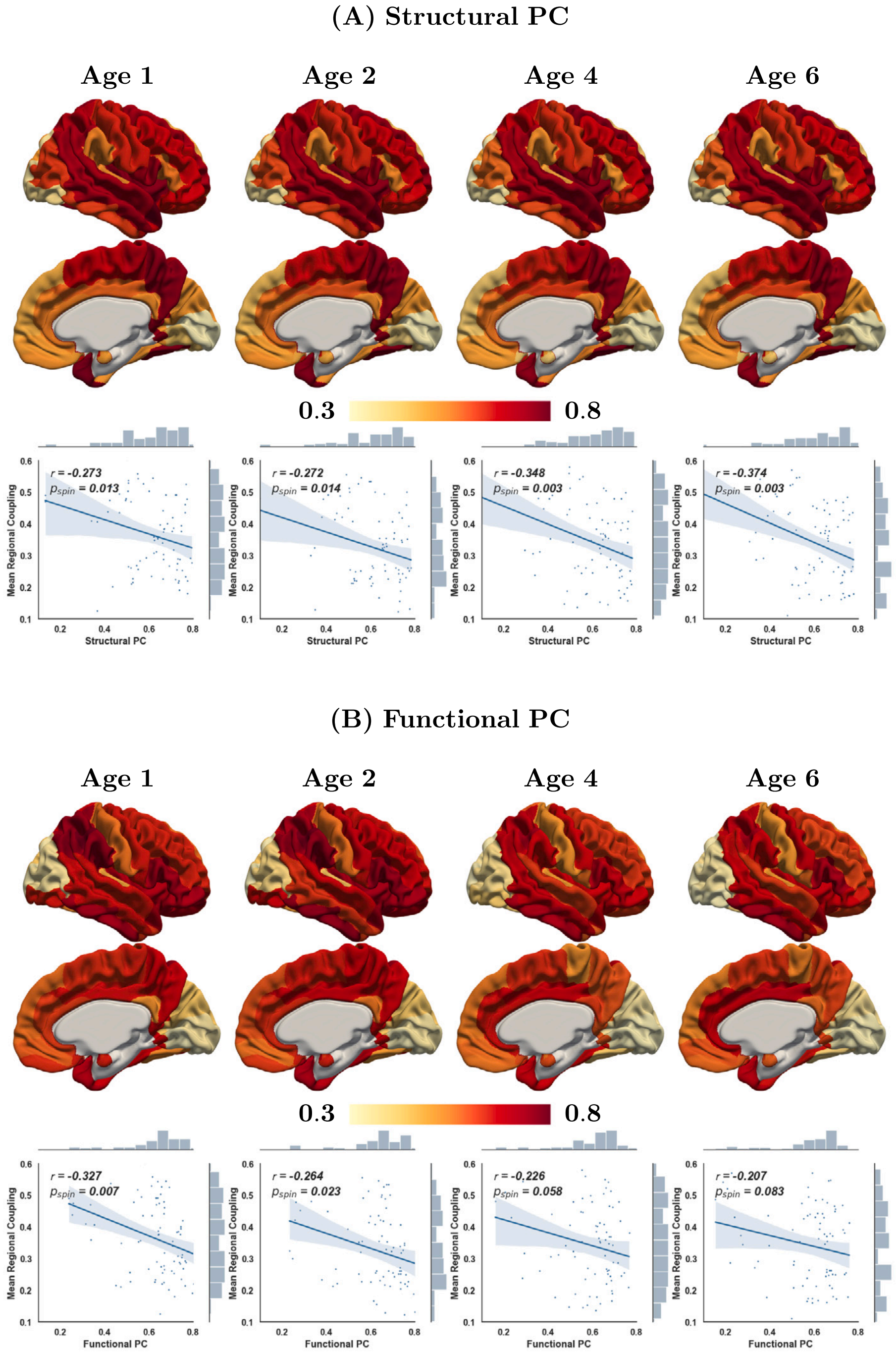

Fig. 6. Participation coefficients for structure (A) and function (B) at each age along with their correlations with S–F coupling. Regions with a high PC exhibit diverse inter-modular connectivity, having relatively low S–F coupling. On the other hand, regions with a lower PC (more localized or segregated connectivity) have relatively high S–F coupling. The significance of correlations was assessed by non-parametric permutation testing (p values are denoted as p_{spin}) (Alexander-Bloch et al., 2018). Note that the scan paradigm was changed from sleep to movie-watching from age 2 to 4.

4. Discussion

Using two different approaches, we found that there is a significant relationship between structural and functional networks in early childhood. We found that cortical S–F coupling in early childhood had regional patterns similar to those observed in adults and that the functional connectome at age 6 could be fairly accurately predicted from the structural connectome at earlier ages using a machine learning approach.

4.1. The patterns of S–F coupling

The strongest S–F coupling in 6 year olds was found in regions involved in default, visual, limbic, ventral attention, and sensorimotor networks. These regions also exhibited the strongest coupling in 4 year olds, and many were also regions of highest S–F coupling in 1 and 2 year olds especially default (L&R Front Med Orb; L&R Ant Cingulum, R Precuneus) and visual regions (L&R Calcarine, R Cuneus).

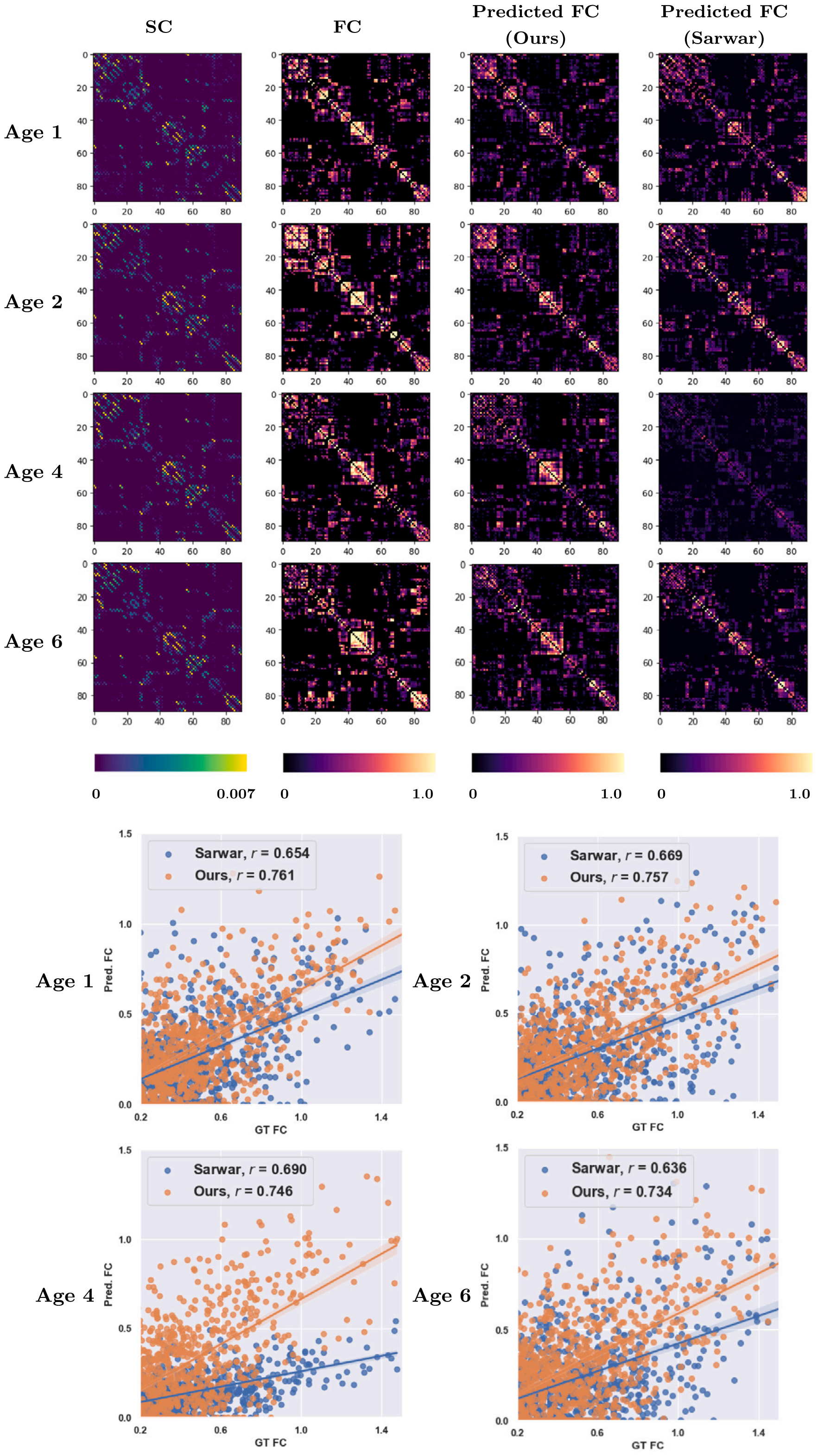

Fig. 7. Representative individual prediction results and prediction correlations from each age. Our methods can predict FC which is close to the ground-truth FC with higher prediction correlation compared to Sarwar's method.

While direct comparison is not possible due to differences in sampling, scanning, and image pre-processing, this regional pattern of S–F coupling is also found in the adults from the HCP study. This may suggest that aspects of adult S–F coupling are already established early in childhood. This general pattern of sensorimotor and default regions having higher S–F coupling compared to other higher-order association

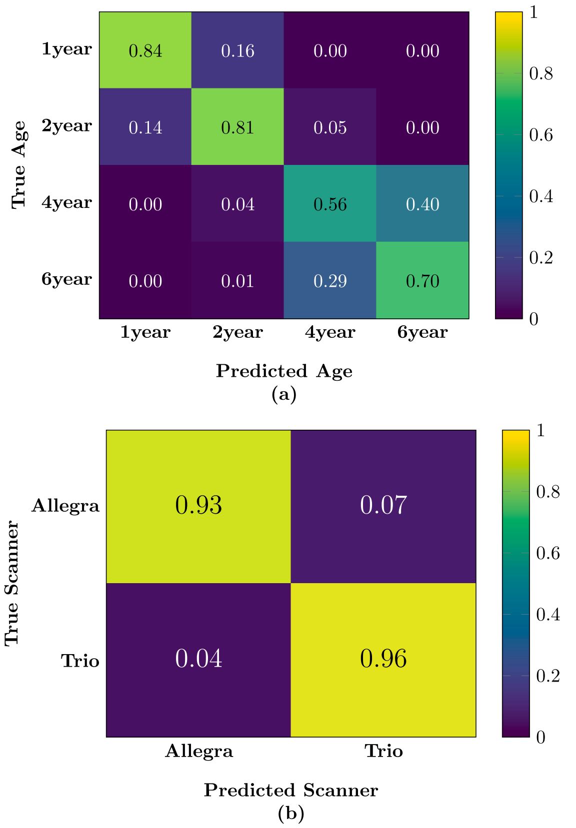

Fig. 8. Age classification (a) and scanner classification results (b). F1 scores for the age classification and the scanner classification are 0.75 and 0.94, respectively.

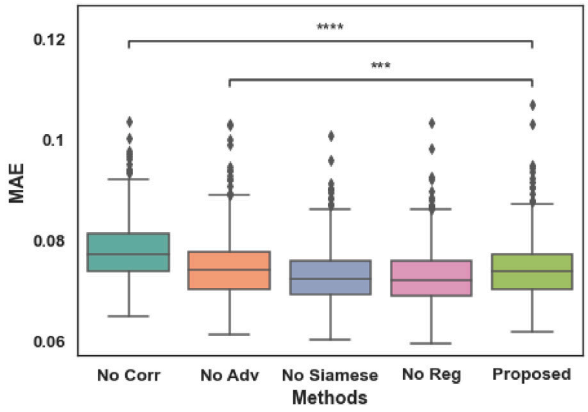

(a) Mean Absolute Error

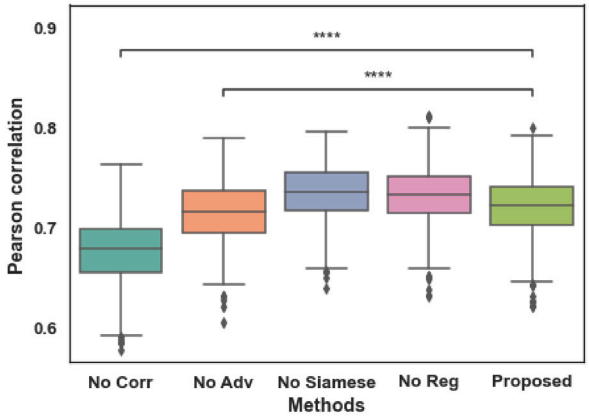

(b) Pearson's correlations

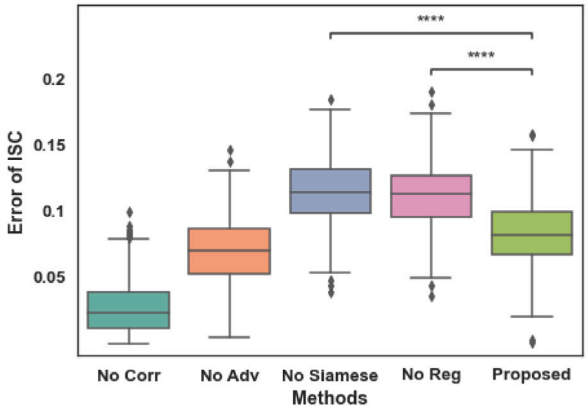

(c) Inter-subject correlations error

Fig. 9. Ablation study: the proposed method shows superior performance compared to the results without correlation loss or without adversarial loss in terms of MAE and Pearson's correlation. The results without Siamese loss or regularization show improved MAE and correlation; however, their inter-subject correlation error is greater than the proposed method. In summary, our proposed method yields prediction results with good inter-subject variability at the cost of a slight reduction of prediction accuracy. *** denotes $0.0001 < p \leq 0.001$ and **** denotes $p \leq 0.0001$.

or transmodal regions is consistent with studies in a sample of 8–23 year olds (Baum et al., 2020) and in adults (Vázquez-Rodríguez et al., 2019; Wang et al., 2019; Preti and Van De Ville, 2019).

Studies in adults have identified several features that contribute to regional heterogeneity of S–F coupling. These include Euclidean distance relationships, cytoarchitecture, myelin content, cell density and functional network hierarchies and gradients (Vázquez-Rodríguez et al., 2019; Wang et al., 2019; Zamani Esfahlani et al., 2022). Many of these cortical features are established by birth or in early postnatal life, so it is not surprising that adult patterns of S–F coupling would be evident in early childhood.

From 1–6 years, we found that most cortical regions experience a decrease or no change in S–F coupling. This is consistent with a recent study in a sample from 7 to 84 years, that found S–F coupling globally tends to decrease with age, especially in sensorimotor regions (Zamani Esfahlani et al., 2022). Zamani Esfahlani et al. (2022) found that simple Euclidean distance and the mean first passage time (a measure of how many steps in a random walk between nodes) were the best predictors of S–F coupling and likely reflected a decentralization of interregional communication with age. Some cortical regions did experience a significant increase in S–F coupling from 1–6 years. These regions tended to be part of the frontoparietal executive network and the visual network. It is interesting that sensory regions and higher order association regions can have similar patterns of S–F coupling development, evidence that the relationship between local and distant connections of a region that underly S–F coupling are complex and heterogeneous (Honey et al., 2009; Hermundstad et al., 2013; Suárez et al., 2020; Liu et al., 2022).

Baum et al. (2020) hypothesized that S–F coupling would be high in the somato-sensory cortex, and low in the transmodal association cortex, which aligns with cortical hierarchies of functional specialization and evolutionary expansion in their cohorts of ages 8–23 years. This spatial variability of S–F coupling is slightly different from our findings, where the primary sensory cortex showed relatively modest coupling. It may be due to different age ranges, different scan protocols and data processing pipelines, or different parcellation labels. However, we observed significantly negative correlations between S–F coupling and PC from both structure and function, which coincides with the findings in Baum et al. (2020).

We found negative correlations between S–F coupling and PC for structural and functional networks in early childhood (though not quite significant at 4 and 6 years for functional networks), suggesting that regions with more local connections have higher S–F coupling than regions with more distributed connections. This pattern is consistent with that found in 8–23 year olds (Baum et al., 2020). However, we found no significant relationships between structural or functional PC and S–F coupling in adults from the HCP study, suggesting that the strength of this relationship may be reduced during maturation of networks later in adolescence.

Given that regional S–F coupling patterns appear to be established early in childhood, S–F coupling may serve as an early imaging biomarker of future cognitive development and risk for psychiatric disorders. For example, S–F coupling in the prefrontal cortex is associated with executive function in adolescents (Baum et al., 2020) and S–F coupling in the reward network at 4.5 years was associated with executive function at 7 and 8.5 years (Chan et al., 2022). Alterations in S–F coupling have also been observed in attention deficit disorder (Soman et al., 2023) and schizophrenia (Wang et al., 2023). Studies of S–F coupling and cognitive development in the EBDS cohort are planned.

4.2. Prediction of the FC from the WM connectome

Our multi-task learning framework provided an accurate prediction of the FC from the SC while preserving inter-subject heterogeneity. Of note, the SC at age 1 accurately predicted the 6 year FC, indicating that the FC is constrained by the SC in early childhood. It is also interesting that the SC at age 1 year was a somewhat better predictor of the FC at age 6 than the year 1 FC. As noted above, major aspects of the WM connectome are present at term and preterm birth (Huang et al., 2015; Bagonis et al., 2022; Ball et al., 2014) and WM hub centrality measures are relatively stable between 1 and 6 years (Bagonis et al., 2022). The FC develops more slowly, with sensorimotor network connections fairly mature by birth, and higher order networks maturing in the first few years of life (Gao et al., 2009; Smyser et al., 2011; Gao et al., 2015). These findings indicate that although functional connections responsible for primary functions essential for early survival (e.g., sensorimotor, auditory, visual, etc.) may become stable/adult-like early on, other higher-order functional connections need prolonged processes for dynamic growth and maturation towards their adult form. However, these dynamic functional processes may be supported by a relatively more stable structural basis. Indeed, a recent study found that the white matter connectome fingerprint in premature infants was stable from 35 weeks until 41 weeks, while the functional connectome fingerprint was not (Ciarrusta et al., 2022). Our findings indicate that the WM connectome sets the stage for future functional connectome development, at least in the first 6 years of life. In this way, the WM connectome may be a more useful early imaging biomarker of future cognition and behavior than the functional connectome, which matures later in childhood, and tends to be more unstable and noisier compared to the structural connectome.

Functional connectivity matrices used in this study were generated from group-level thresholding with $p < 0.01$. The prediction results for FCs with different strategies (group-level thresholding and individual-level thresholding) and different p values are summarized in Fig. S9. Our prediction model is able to generate individual FC based on their SC regardless of different thresholding strategies and levels. For individual-level thresholded FCs, the correlation is lower and the error is higher than for group-level thresholded FCs.

Our multi-task learning framework provided the accurate prediction of FCs while preserving the inter-subject heterogeneity. We also proposed new loss functions to control the trade-off between the prediction accuracy and the prediction heterogeneity. Note that in Sarwar et al. (2021), there were two parameters to control inter-subject variability: λ as regularization constant and γ as inter-subject correlations of the training samples. Simple average FC across the whole population can be a good representative predictor without any effort to train a prediction model. However, it does not capture inter-subject variability so that the predicted FC is not discriminative in different individuals.

We observed that several subjects' FC matrices were harder to predict from their SC for both our method and Sarwar's method. We will investigate whether these outliers are related to cognitive performance or behavioral differences. As previously studied in Sarwar et al. (2021), instead of SC or the ground-truth FC, the predicted FC can be used to investigate the relationships between brain function and inter-subject variations in cognition and behavior. As functional connectomes capture more inter-subject variations in behavior than structural connectomes (Seguin et al., 2020; Sarwar et al., 2021), the predicted FC may enable us to predict individual cognitive performance or explain behavioral differences.

In this study, SC and FC matrices were generated from 90 × 90 AAL parcellation labels. In the future, we will reconstruct the connectome matrices from different parcellation labels with different number of nodes to see the effect of different templates, for example, Desikan–Killiany parcellation (Desikan et al., 2006) or 400-region cortical parcellation (Schaefer et al., 2018) used in Baum et al. (2020) as it is known that there is a significant effect of different brain parcellation in structure-function relationship (Messé, 2020). We did not investigate the prediction of SC from FC in this study, as our hypothesis is that structure precedes function in early brain development. We will investigate the prediction of SC from FC more in future studies.

In summary, in this work, we quantified and characterized the degree of regional profiles of structure and function in early childhood. We found that average regional structure-function coupling remains relatively stable at ages 1, 2, 4, and 6. We developed an individual prediction deep learning model based on graph convolutional neural networks and demonstrated that it is possible to generate individual functional connectivity from their structural connectome while preserving inter-subject variability.

Declaration of competing interest

The authors declare that they have no known competing financial interests or personal relationships that could have appeared to influence the work reported in this paper.

Data availability

Some of the raw structural and diffusion MRI images for EBDS are available in NIMH Data Archive (NDA).

Funding

This work was supported by National Institutes of Health (R01 MH123747, R01 MH070890, R01 HD053000, R01 MH064065 to J.H.G.; R01 HD055741, P50 HD103573, R01 MH118362 to M.A.S.; T32 MH106440 to M.B.).

Appendix A. Supplementary data

Supplementary material related to this article can be found online at https://doi.org/10.1016/j.dcn.2023.101314.

References

Alexander-Bloch, A.F., Shou, H., Liu, S., Satterthwaite, T.D., Glahn, D.C., Shinohara, R.T., Vandekar, S.N., Raznahan, A., 2018. On testing for spatial correspondence between maps of human brain structure and function. Neuroimage 178, 540–551.

Avants, B.B., Epstein, C.L., Grossman, M., Gee, J.C., 2008. Symmetric diffeomorphic image registration with cross-correlation: evaluating automated labeling of elderly and neurodegenerative brain. Med. Image Anal. 12 (1), 26–41.

Bagonis, M., Cornea, E., Girault, J.B., Stephens, R.L., Kim, S., Prieto, J.C., Styner, M., Gilmore, J.H., 2022. Early childhood development of node centrality in the white matter connectome and its relationship to IQ at 6 years. Biol. Psychiatry Cogn. Neurosci. Neuroimaging.

Ball, G., Aljabar, P., Zebari, S., Tusor, N., Arichi, T., Merchant, N., Robinson, E.C., Ogundipe, E., Rueckert, D., Edwards, A.D., et al., 2014. Rich-club organization of the newborn human brain. Proc. Natl. Acad. Sci. 111 (20), 7456–7461.

Battaglia, P.W., Hamrick, J.B., Bapst, V., Sanchez-Gonzalez, A., Zambaldi, V., Malinowski, M., Tacchetti, A., Raposo, D., Santoro, A., Faulkner, R., et al., 2018. Relational inductive biases, deep learning, and graph networks. arXiv preprint arXiv:1806.01261.

Baum, G.L., Cui, Z., Roalf, D.R., Ciric, R., Betzel, R.F., Larsen, B., Cieslak, M., Cook, P.A., Xia, C.H., Moore, T.M., et al., 2020. Development of structure–function coupling in human brain networks during youth. Proc. Natl. Acad. Sci. 117 (1), 771–778.

Behrens, T.E., Berg, H.J., Jbabdi, S., Rushworth, M.F., Woolrich, M.W., 2007. Probabilistic diffusion tractography with multiple fibre orientations: What can we gain? Neuroimage 34 (1), 144–155.

Benjamini, Y., Hochberg, Y., 1995. Controlling the false discovery rate: a practical and powerful approach to multiple testing. J. R. Stat. Soc. B 57 (1), 289–300.

Besson, P., Lopes, R., Leclerc, X., Derambure, P., Tyvaert, L., 2014. Intra-subject reliability of the high-resolution whole-brain structural connectome. NeuroImage 102, 283–293.

Chan, S.Y., Ong, Z.Y., Ngoh, Z.M., Chong, Y.S., Zhou, J.H., Fortier, M.V., Daniel, L.M., Qiu, A., Meaney, M.J., Tan, A.P., 2022. Structure-function coupling within the reward network in preschool children predicts executive functioning in later childhood. Dev. Cogn. Neurosci. 55, 101107.

Cheng, J., Wang, Z., Pollastri, G., 2008. A neural network approach to ordinal regression. In: 2008 IEEE International Joint Conference on Neural Networks (IEEE World Congress on Computational Intelligence). IEEE, pp. 1279–1284.

Ciarrusta, J., Christiaens, D., Fitzgibbon, S.P., Dimitrova, R., Hutter, J., Hughes, E., Duff, E., Price, A.N., Cordero-Grande, L., Tournier, J.D., et al., 2022. The developing brain structural and functional connectome fingerprint. Dev. Cogn. Neurosci. 101117.

Cox, R.W., 1996. AFNI: software for analysis and visualization of functional magnetic resonance neuroimages. Comput. Biomed. Res. 29 (3), 162–173.

Dale, A.M., Fischl, B., Sereno, M.I., 1999. Cortical surface-based analysis: I. Segmentation and surface reconstruction. Neuroimage 9 (2), 179–194.

Defferrard, M., Bresson, X., Vandergheynst, P., 2016. Convolutional neural networks on graphs with fast localized spectral filtering. Adv. Neural Inf. Process. Syst. 29.

Desikan, R.S., Ségonne, F., Fischl, B., Quinn, B.T., Dickerson, B.C., Blacker, D., Buckner, R.L., Dale, A.M., Maguire, R.P., Hyman, B.T., et al., 2006. An automated labeling system for subdividing the human cerebral cortex on MRI scans into gyral based regions of interest. Neuroimage 31 (3), 968–980.

Dubois, J., Dehaene-Lambertz, G., Kulikova, S., Poupon, C., Hüppi, P.S., Hertz-Pannier, L., 2014. The early development of brain white matter: a review of imaging studies in fetuses, newborns and infants. Neuroscience 276, 48–71.

Fortin, J.P., Cullen, N., Sheline, Y.I., Taylor, W.D., Aselcioglu, I., Cook, P.A., Adams, P., Cooper, C., Fava, M., McGrath, P.J., et al., 2018. Harmonization of cortical thickness measurements across scanners and sites. Neuroimage 167, 104–120.

Gao, W., Alcauter, S., Elton, A., Hernandez-Castillo, C.R., Smith, J.K., Ramirez, J., Lin, W., 2015. Functional network development during the first year: relative sequence and socioeconomic correlations. Cerebral Cortex 25 (9), 2919–2928.

Gao, W., Lin, W., Grewen, K., Gilmore, J.H., 2017. Functional connectivity of the infant human brain: plastic and modifiable. Neuroscientist 23 (2), 169–184.

Gao, W., Zhu, H., Giovanello, K.S., Smith, J.K., Shen, D., Gilmore, J.H., Lin, W., 2009. Evidence on the emergence of the brain's default network from 2-week-old to 2-year-old healthy pediatric subjects. Proc. Natl. Acad. Sci. 106 (16), 6790–6795.

Geng, X., Gouttard, S., Sharma, A., Gu, H., Styner, M., Lin, W., Gerig, G., Gilmore, J.H., 2012. Quantitative tract-based white matter development from birth to age 2 years. Neuroimage 61 (3), 542–557.

Gilmore, J.H., Knickmeyer, R.C., Gao, W., 2018. Imaging structural and functional brain development in early childhood. Nat. Rev. Neurosci. 19 (3), 123–137.

Glasser, M.F., Coalson, T.S., Robinson, E.C., Hacker, C.D., Harwell, J., Yacoub, E., Ugurbil, K., Andersson, J., Beckmann, C.F., Jenkinson, M., et al., 2016. A multi-modal parcellation of human cerebral cortex. Nature 536 (7615), 171–178.

Glasser, M.F., Sotiropoulos, S.N., Wilson, J.A., Coalson, T.S., Fischl, B., Andersson, J.L., Xu, J., Jbabdi, S., Webster, M., Polimeni, J.R., et al., 2013. The minimal preprocessing pipelines for the human connectome project. Neuroimage 80, 105–124.

Goodfellow, I., Pouget-Abadie, J., Mirza, M., Xu, B., Warde-Farley, D., Ozair, S., Courville, A., Bengio, Y., 2014. Generative adversarial nets. Adv. Neural Inf. Process. Syst. 27.

Guimera, R., Amaral, L.A.N., 2005. Cartography of complex networks: modules and universal roles. J. Stat. Mech. Theory Exp. 2005 (02), P02001.

Hagmann, P., Cammoun, L., Gigandet, X., Meuli, R., Honey, C.J., Wedeen, V.J., Sporns, O., 2008. Mapping the structural core of human cerebral cortex. PLoS Biol. 6 (7), e159.

Hermundstad, A.M., Bassett, D.S., Brown, K.S., Aminoff, E.M., Clewett, D., Freeman, S., Frithsen, A., Johnson, A., Tipper, C.M., Miller, M.B., et al., 2013. Structural foundations of resting-state and task-based functional connectivity in the human brain. Proc. Natl. Acad. Sci. 110 (15), 6169–6174.

Honey, C.J., Sporns, O., Cammoun, L., Gigandet, X., Thiran, J.P., Meuli, R., Hagmann, P., 2009. Predicting human resting-state functional connectivity from structural connectivity. Proc. Natl. Acad. Sci. 106 (6), 2035–2040.

Huang, H., Shu, N., Mishra, V., Jeon, T., Chalak, L., Wang, Z.J., Rollins, N., Gong, G., Cheng, H., Peng, Y., et al., 2015. Development of human brain structural networks through infancy and childhood. Cerebral Cortex 25 (5), 1389–1404.

Jbabdi, S., Sotiropoulos, S.N., Savio, A.M., Graña, M., Behrens, T.E., 2012. Model-based analysis of multishell diffusion MR data for tractography: How to get over fitting problems. Magn. Reson. Med. 68 (6), 1846–1855.

Johansen-Berg, H., Behrens, T.E., 2013. Diffusion MRI: From Quantitative Measurement to in Vivo Neuroanatomy. Academic Press.

Johnson, H., Harris, G., Williams, K., et al., 2007. BRAINSFit: mutual information rigid registrations of whole-brain 3D images, using the insight toolkit. Insight J. 57 (1), 1–10.

Kim, J.S., Singh, V., Lee, J.K., Lerch, J., Ad-Dab'bagh, Y., MacDonald, D., Lee, J.M., Kim, S.I., Evans, A.C., 2005. Automated 3-D extraction and evaluation of the inner and outer cortical surfaces using a Laplacian map and partial volume effect classification. Neuroimage 27 (1), 210–221.

Kipf, T.N., Welling, M., 2016. Semi-supervised classification with graph convolutional networks. arXiv preprint arXiv:1609.02907.

Li, Y., Mateos, G., Zhang, Z., 2021. Learning to model the relationship between brain structural and functional connectomes. arXiv preprint arXiv:2112.09906.

Lin, T.Y., Goyal, P., Girshick, R., He, K., Dollár, P., 2017. Focal loss for dense object detection. In: Proceedings of the IEEE International Conference on Computer Vision. pp. 2980–2988.

Liu, Z.Q., Vazquez-Rodriguez, B., Spreng, R.N., Bernhardt, B.C., Betzel, R.F., Misic, B., 2022. Time-resolved structure-function coupling in brain networks. Commun. Biol. 5 (1), 532.

Liu, M., Zhang, J., Adeli, E., Shen, D., 2018. Joint classification and regression via deep multi-task multi-channel learning for Alzheimer's disease diagnosis. IEEE Trans. Biomed. Eng. 66 (5), 1195–1206.

Messé, A., 2020. Parcellation influence on the connectivity-based structure–function relationship in the human brain. Hum. Brain Mapp. 41 (5), 1167–1180.

Neudorf, J., Kress, S., Borowsky, R., 2022. Structure can predict function in the human brain: a graph neural network deep learning model of functional connectivity and centrality based on structural connectivity. Brain Struct. Funct. 227 (1), 331–343.

Oguz, I., Farzinfar, M., Matsui, J., Budin, F., Liu, Z., Gerig, G., Johnson, H.J., Styner, M., 2014. DTIPrep: quality control of diffusion-weighted images. Front. Neuroinformatics 8, 4.

Ouyang, M., Dubois, J., Yu, Q., Mukherjee, P., Huang, H., 2019. Delineation of early brain development from fetuses to infants with diffusion MRI and beyond. Neuroimage 185, 836–850.

Passingham, R.E., Stephan, K.E., Kötter, R., 2002. The anatomical basis of functional localization in the cortex. Nat. Rev. Neurosci. 3 (8), 606–616.

Pham, K., Yang, X., Niethammer, M., Prieto, J.C., Styner, M., 2019. Multiseg pipeline: automatic tissue segmentation of brain MR images with subject-specific atlases. In: Medical Imaging 2019: Biomedical Applications in Molecular, Structural, and Functional Imaging, Vol. 10953. SPIE, pp. 97–102.

Piot, E., Bagonis, M., Wu, G., Prieto, J.C., Styner, M., 2022. CONTINUITY: CONnectivity tool with INtegration of subcortical regions, registration and visualization of tractography. In: Medical Imaging 2022: Biomedical Applications in Molecular, Structural, and Functional Imaging, Vol. 12036. SPIE, pp. 22–28.

Power, J.D., Barnes, K.A., Snyder, A.Z., Schlaggar, B.L., Petersen, S.E., 2012. Spurious but systematic correlations in functional connectivity MRI networks arise from subject motion. Neuroimage 59 (3), 2142–2154.

Power, J.D., Mitra, A., Laumann, T.O., Snyder, A.Z., Schlaggar, B.L., Petersen, S.E., 2014. Methods to detect, characterize, and remove motion artifact in resting state fMRI. Neuroimage 84, 320–341.

Preti, M.G., Van De Ville, D., 2019. Decoupling of brain function from structure reveals regional behavioral specialization in humans. Nat. Commun. 10 (1), 4747.

Sadeghi, N., Prastawa, M., Fletcher, P.T., Wolff, J., Gilmore, J.H., Gerig, G., 2013. Regional characterization of longitudinal DT-MRI to study white matter maturation of the early developing brain. Neuroimage 68, 236–247.

Sarwar, T., Tian, Y., Yeo, B.T., Ramamohanarao, K., Zalesky, A., 2021. Structure-function coupling in the human connectome: A machine learning approach. NeuroImage 226, 117609.

Schaefer, A., Kong, R., Gordon, E.M., Laumann, T.O., Zuo, X.N., Holmes, A.J., Eickhoff, S.B., Yeo, B.T., 2018. Local-global parcellation of the human cerebral cortex from intrinsic functional connectivity MRI. Cerebral Cortex 28 (9), 3095–3114.

Seguin, C., Tian, Y., Zalesky, A., 2020. Network communication models improve the behavioral and functional predictive utility of the human structural connectome. Netw. Neurosci. 4 (4), 980–1006.

Shi, F., Yap, P.T., Wu, G., Jia, H., Gilmore, J.H., Lin, W., Shen, D., 2011. Infant brain atlases from neonates to 1-and 2-year-olds. PLoS One 6 (4), e18746.

Smith, S.M., 2002. Fast robust automated brain extraction. Human Brain Mapp. 17 (3), 143–155.

Smith, S.M., Jenkinson, M., Woolrich, M.W., Beckmann, C.F., Behrens, T.E., Johansen-Berg, H., Bannister, P.R., De Luca, M., Drobnjak, I., Flitney, D.E., et al., 2004. Advances in functional and structural MR image analysis and implementation as FSL. Neuroimage 23, S208–S219.

Smyser, C.D., Snyder, A.Z., Neil, J.J., 2011. Functional connectivity MRI in infants: exploration of the functional organization of the developing brain. Neuroimage 56 (3), 1437–1452.

Soman, S.M., Vijayakumar, N., Thomson, P., Ball, G., Hyde, C., Silk, T.J., 2023. Cortical structural and functional coupling during development and implications for attention deficit hyperactivity disorder. Transl. Psychiatry 13 (1), 252.

Stephens, R.L., Langworthy, B.W., Short, S.J., Girault, J.B., Styner, M.A., Gilmore, J.H., 2020. White matter development from birth to 6 years of age: a longitudinal study. Cerebral Cortex 30 (12), 6152–6168.

Suárez, L.E., Markello, R.D., Betzel, R.F., Misic, B., 2020. Linking structure and function in macroscale brain networks. Trends Cogn. Sci. 24 (4), 302–315.

Van Essen, D.C., Smith, S.M., Barch, D.M., Behrens, T.E., Yacoub, E., Ugurbil, K., Wu-Minn HCP Consortium, et al., 2013. The WU-Minn human connectome project: an overview. Neuroimage 80, 62–79.

Vázquez-Rodríguez, B., Suárez, L.E., Markello, R.D., Shafiei, G., Paquola, C., Hagmann, P., Van Den Heuvel, M.P., Bernhardt, B.C., Spreng, R.N., Misic, B., 2019. Gradients of structure–function tethering across neocortex. Proc. Natl. Acad. Sci. 116 (42), 21219–21227.

Wang, B., Guo, M., Pan, T., Li, Z., Li, Y., Xiang, J., Cui, X., Niu, Y., Yang, J., Wu, J., et al., 2023. Altered higher-order coupling between brain structure and function with embedded vector representations of connectomes in schizophrenia. Cerebral Cortex 33 (9), 5447–5456.

Wang, P., Kong, R., Kong, X., Liégeois, R., Orban, C., Deco, G., Van Den Heuvel, M.P., Thomas Yeo, B., 2019. Inversion of a large-scale circuit model reveals a cortical hierarchy in the dynamic resting human brain. Sci. Adv. 5 (1), eaat7854.

Yeo, B.T., Krienen, F.M., Sepulcre, J., Sabuncu, M.R., Lashkari, D., Hollinshead, M., Roffman, J.L., Smoller, J.W., Zöllei, L., Polimeni, J.R., et al., 2011. The organization of the human cerebral cortex estimated by intrinsic functional connectivity. J. Neurophysiology.

Zamani Esfahlani, F., Faskowitz, J., Slack, J., Mišić, B., Betzel, R.F., 2022. Local structure-function relationships in human brain networks across the lifespan. Nat. Commun. 13 (1), 2053.

Zhang, L., Wang, L., Zhu, D., Alzheimer's Disease Neuroimaging Initiative, et al., 2022. Predicting brain structural network using functional connectivity. Med. Image Anal. 79, 102463.